Journal of Electronic Materials (2021) 50:3819–3835
https://doi.org/10.1007/s11664-021-08908-6

ORIGINAL RESEARCH ARTICLE

Comprehensive Studies on Steady-State and Transient Electronic Transport in $In_{0.52}Al_{0.48}As$

Anup Kumar Mandia[1] · Bhaskaran Muralidharan[1] · Seung Cheol Lee[2] · Satadeep Bhattacharjee[2]

Received: 27 October 2020 / Accepted: 25 March 2021 / Published online: 15 April 2021
© The Minerals, Metals & Materials Society 2021

Abstract

High electron mobility transistors built using $In_{0.52}Al_{0.48}As/In_{0.53}Ga_{0.47}As$ on InP substrates are currently being investigated for numerous applications due to their favorable performance for microwave, optical and digital applications. We present a detailed and comprehensive study of steady-state and transient electronic transport in $In_{0.52}Al_{0.48}As$ with a three-valley model using the semi-classical ensemble Monte Carlo method including all important scattering mechanisms. Electronic transport parameters such as drift velocity, valley occupation, average electron energy, ionization coefficient and generation rate, electron effective mass, diffusion coefficient, energy and momentum relaxation time are extracted rigorously from the simulations. Using these, we present a detailed characterization of the transient electronic transport showing the variation of drift velocity with distance and time. We further estimate the optimal cut-off frequencies for various device lengths via the velocity overshoot effect. Our analysis shows that transient effects are significant for device lengths shorter than 700 nm and should be taken into account for optimal device designs. As a critical example at length scales of around 100 nm, we obtain a significant improvement in the cut-off frequency from 261 GHz to 663 GHz with the inclusion of transient effects. The field dependence of all extracted parameters done here can prove to be highly useful for further device analysis and design.

Keywords Ensemble Monte Carlo · transient · relaxation time · diffusivity

Introduction

High electron mobility transistors (HEMT) built using heterostructures of $In_{0.52}Al_{0.48}As/In_{0.53}Ga_{0.47}As$ on InP substrates have been of great interest in experimental studies due to their favourable performance in microwave, optical and digital applications.[1–15] Laser and charge injection transistors (CHINT)[16,17] fabricated from such material systems have also shown promising device performance characteristics such that InAlAs/InGaAs/InP structures are considered to be preferable, owing to better integration with better power efficiency, faster speed, high-frequency gain, low noise, and low cost.

✉ Satadeep Bhattacharjee
s.bhattacharjee@ikst.res.in

Seung Cheol Lee
seungcheol.lee@ikst.res.in

1 Department of Electrical Engineering, Indian Institute of Technology Bombay, Powai, Mumbai 400076, India

2 Indo Korea Science and Technology Center, Bangalore 560065, India

HEMTs based on $In_{0.52}Al_{0.48}As/In_{0.53}Ga_{0.47}As/InP$ have a cut-off frequency higher than 600 GHz and are considered to be among the fastest transistors.[18,19] These HEMTs have also shown significant capabilities for cryogenic operations in terms of improved noise characteristics.[15,20–27] Such HEMT structures coupled with GaAs and InAs have also shown good device performances[28–35] suitable for various digital and analog applications. To exploit the avenues for application from these structures, a deeper understanding of electronic transport across these structures is necessary. While there are already a number of experimental and theoretical studies for InP and $In_{0.53}Ga_{0.47}As$, very little information is available for the $In_{0.52}Al_{0.48}As$ system in terms of material parameters and transport properties. The objective of this paper is to present a detailed and comprehensive study of steady-state and transient electronic transport in $In_{0.52}Al_{0.48}As$ with the three-valley model using the semi-classical ensemble Monte Carlo method and including all important scattering mechanisms. In our model, all electronic transport parameters such drift velocity, valley occupation, average electron energy, ionization coefficient and generation rate,

electron effective mass, diffusion coefficient, and energy and momentum relaxation time are extracted rigorously from the simulations.

There are a wide variety of semi-classical transport models[36–69] used to understand transport physics. Amongst them, the Monte Carlo method[54,55] is considered to be most accurate with easy implementation, providing better insights from a physical point of view and has been widely used[54–59] for transport calculations. The accuracy of these methods are limited only by the models used to calculate the band structure and the scattering rate.

For larger device dimensions, an understanding of steady-state transport is sufficient. In smaller devices, transient transport is also essential when estimating device performance. Transient electronic transport in short-channel FETs was first studied by Ruch.[70] It was shown that the transient electron drift velocity may exceed the steady-state drift velocity by a proper selection of the electric field. The first experimental studies on transient electronic transport was done by Heiblum et.al.[71] in GaAs. Later, many investigations on transient transport were performed both theoretically and experimentally[72–76] for a wide class of materials.

Electronic transport properties in $In_{0.52}Al_{0.48}As$ were earlier analysed only in the steady state[77,78] by using Monte Carlo methods. A previous study had also shown that electron transit time in $In_{0.52}Al_{0.48}As$ layer is the main factor that decides the total device transit time for CHINT[16] applications. Therefore, for the fabrication of high-speed devices as well as ultra-short devices, it is necessary to analyse the transient electronic transport. In this work, our initial focus is on the examination of steady state transport, by studying the variation of the drift velocity with the electric field, the temperature and the doping concentration. Next, the variation in electron energy, electron occupancy in different bands with electric field is discussed. The variation of the impact ionization coefficient and the generation rate with electric fields is also examined. The variation of the diffusion coefficient and the momentum and energy relaxation time with electric field and temperature are also presented. Using these, we present a detailed characterization of the transient electronic transport showing the variation of drift velocity with distance and time. We then estimate optimal cut-off frequencies for various device lengths via the velocity overshoot effect. Our analysis shows that for device lengths shorter than 700 nm, transient effects are significant and should be taken into account for optimal device designs. As a critical example, at length scales of around 100 nm, we obtain a significant improvement in the cut-off frequency from 261 GHz to 663 GHz with the inclusion of transient effects. Finally, device implications of our results are discussed and the upper bound cut-off frequencies for device optimization are calculated for short channel high frequency electronic device applications.

This paper is organized as follows: In the following section, the Monte Carlo procedure is discussed and the related parameters required to study transport in $In_{0.52}Al_{0.48}As$ are presented in detail. Furthermore, the methodology for calculating the diffusion constant and momentum and energy relaxation times is discussed in detail. In "Results and Discussion" section, the results of our simulations are discussed thoroughly. First, we discuss the velocity-field characteristics in n-type $In_{0.52}Al_{0.48}As$ for different temperatures and doping concentrations. Then, the variation of the diffusion coefficient, the momentum and energy relaxation times with electric field and temperature are presented. Next, the transient electronic transport

Table I The material parameters for bulk $In_{0.52}Al_{0.48}As$

Parameter	Value
Bulk material parameters	
Polar optical phonon energy (eV)	0.0397
Low-frequency dielectric constant ϵ_s	12.414
High-frequency dielectric constant ϵ_∞	10.072
Energy band gap E_g (eV)	1.44
Density ρ (kg/m^3)	4753
Acoustic deformation potential D_{ac} (eV)	7.936
Sound velocity v_s (m/s)	4.998×10^3
Piezoelectric constant (P_{pz})	0.048069
Alloy scattering potential (eV)	0.47
Elastic constants	
c_{11} (N/m^2)	1.01×10^{11}
c_{12} (N/m^2)	5.11×10^{10}
c_{44} (N/m^2)	4.78×10^{10}

Table II Valley-dependent parameters for bulk $In_{0.52}Al_{0.48}As$

Parameters	Γ	*L*	*X*
Effective mass m*	0.08396	0.39	0.602
Non-parabolicity α (eV^{-1})	0.58273	0.20904	0.066556
Valley separation (eV)	—	0.34	0.6
Number of equivalent valleys	1	4	3
Optical phonon energy			
E_{op} (eV)	0.0397	0.0397	0.0397
Intervalley deformation			
Potential D_i (eV/m)			
From Γ	0	5.37×10^{10}	5.7×10^{10}
From L	5.37×10^{10}	4.95×10^{10}	5.18×10^{10}
From X	5.7×10^{10}	5.18×10^{10}	4.21×10^{10}
Intervalley phonon energy (eV)			
From Γ	0	0.043	0.043
From *L*	0.043	0.043	0.0411
From *X*	0.043	0.041	0.043

as a function of both length and time are discussed. Following this, the device implications of our results is discussed. Finally, "Conclusion" section summarizes the important conclusions of this paper.

Simulation Setup and Formulation

Monte Carlo Procedure

We study electron transport in bulk $In_{0.52}Al_{0.48}As$ using the ensemble Monte Carlo method. We use a three-valley model for the conduction band structure of the electrons. For Monte Carlo simulation we use a time step of 10 fs and for steady-state analysis we maintain the simulation for 100 ps. Further details the Monte Carlo method are given in other references.[55,57,79] The band structure is treated by using a non-parabolic model,[80] with a dispersion relation given by

$$E(k)(1+\alpha E(k))=\gamma(E(k))=\frac{\hbar^2k^2}{2m^*}, \quad (1)$$

where k is the wave vector, $E(k)$ is the energy of a particle of wave vector k, $\hbar$ is the reduced Planck constant, and α is a non-parabolic coefficient given by

$$\alpha=\frac{1}{E_g}\left(1-\frac{m^*}{m_0}\right)^2, \quad (2)$$

where E_g is the energy band gap, m^* is the effective mass of an electron at the bottom of the band and m_0 is the free electron mass. For both steady-state and transient analysis, 10,000 electrons are considered. We assume that all donors are ionized and the free-electron concentration is equal to the donor concentration. In all cases, the doping concentration is set to $1\times10^{22}m^{-3}$, unless mentioned explicitly. The material parameters used in the calculation for bulk $In_{0.52}Al_{0.48}As$ are listed in Tables I and II. For the required alloy compositions, all values are linearly extrapolated between the material parameters of AlAs and InAs.[81]

Scattering Mechanisms

In the present work, we consider the following scattering mechanisms: ionized impurity scattering, polar optical phonon scattering, piezoelectric scattering, acoustic phonon scattering, alloy scattering, non-equivalent and equivalent intervalley scattering, and finally, impact ionization scattering. We now proceed to discuss all scattering mechanisms and their implementation in detail.

Ionized Impurity Scattering

Ionized impurity scattering is an important scattering mechanism at high doping concentrations specifically at low temperatures. The ionized impurity scattering mechanism is considered an elastic and anisotropic scattering mechanism whose scattering rate is given by[82]

$$W(E)=\frac{\sqrt{2}e^4N_Im^{*3/2}}{\pi\epsilon_s^2\hbar^4}\left(\sqrt{E(1+\alpha E)}(1+2\alpha E)\right)\left(\frac{1}{q_D^2\left(q_D^2+\frac{8m^*E(1+\alpha E)}{\hbar^2}\right)}\right), \quad (3)$$

where q_D is inverse screening length given by

$$q_D=\sqrt{\frac{e^2N_I}{\epsilon_sk_BT}}, \quad (4)$$

where N_I is the donor concentration, e is the electronic charge, ϵ_s is the low-frequency dielectric constant, k_B is the Boltzmann constant and T is the temperature. The angle θ between the initial wave-vector $\boldsymbol{k}$ and the final wave-vector $\boldsymbol{k}'$ after ionized impurity scattering, is given by[83]

$$cos\theta=1-\frac{2(1-r)}{1-r(\frac{4k^2}{q_D^2})} \quad (5)$$

where r is a uniformly distributed random number between 0 and 1.

Polar Optical Phonon Scattering

Typically, polar optical phonon scattering is a dominant scattering mechanism near room temperature and in the higher temperature region. Polar optical phonon scattering is an inelastic and an anisotropic scattering mechanism. The scattering rate for polar optical phonon scattering is given by[55]

$$W(E)=\frac{e^2\sqrt{m^*}\omega_{op}}{\sqrt{2}\hbar}\left(\frac{1}{\epsilon_\infty}-\frac{1}{\epsilon_s}\right)\frac{1+2\alpha E'}{\sqrt{E(1+\alpha E)}}F_0(E,E')\times\begin{Bmatrix}N_0 & (absorption)\\(N_0+1) & (emission)\end{Bmatrix} \quad (6)$$

where

$$F_0(E,E')=C^{-1}\left[Aln\left|\frac{\sqrt{\gamma(E)}+\sqrt{\gamma(E')}}{\sqrt{\gamma(E)}-\sqrt{\gamma(E')}}\right|+B\right] \quad (7)$$

$$A = \left\{2(1+\alpha E)(1+\alpha E^{'}) + \alpha[\gamma(E)+\gamma(E')]\right\}^2 \tag{8}$$

$$B = -2\alpha\sqrt{\gamma(E)\gamma(E^{'})}\left[4(1+\alpha E)(1+\alpha E^{'}) + \alpha\left\{\gamma(E)+\gamma(E^{'})\right\}\right] \tag{9}$$

$$C = 4(1+\alpha E)(1+\alpha E^{'})(1+2\alpha E)(1+2\alpha E^{'}) \tag{10}$$

where ϵ_∞ is the high-frequency dielectric constant, ω_{op} is the polar optical phonon frequency, $E^{'} = E + \hbar\omega_{op}$ for absorption and $E^{'} = E - \hbar\omega_{op}$ for emission of a polar optical phonon, if $E^{'} < 0$ polar optical phonon scattering will not occur, N_0 is the number of phonons involved in the transition. N_0 is given by

$$N_0 = \frac{1}{e^{\frac{\hbar\omega_{op}}{k_B T}} - 1} \tag{11}$$

The angle θ between the initial wave-vector $\boldsymbol{k}$ and final wave-vector $\boldsymbol{k'}$ for polar optical phonon scattering is given by the following probability distribution function[84,85]

$$P(cos\theta)d(cos\theta) = a_{pop}\frac{(\sqrt{\gamma(E)\gamma(E^{'})} + \alpha EE^{'}cos\theta)^2}{\gamma(E)+\gamma(E^{'}) - 2\sqrt{\gamma(E)\gamma(E^{'})}cos\theta}d(cos\theta) \tag{12}$$

where a_{pop} is a normalization constant. The random values of $cos\theta$ with the above probability distribution are obtained by using von-Neumann rejection.[84,86]

Piezoelectric Scattering

Piezoelectric scattering is an important scattering mechanism at low doping density and low temperature in polar materials. Piezoelectric scattering is treated here using elastic and equipartition approximation. The piezoelectric scattering rate is given by[87,88]

$$W(E) = \frac{m^{*^{1/2}}e^2P_{pz}^2k_BT}{4\sqrt{2}\pi\hbar^2\epsilon_s}\left(\frac{1+2\alpha E}{\sqrt{E(1+\alpha E)}}\right)ln\left(1+\frac{8m^*E(1+\alpha E)}{\hbar^2q_D^2}\right) \tag{13}$$

where P_{pz} is a dimensionless piezoelectric coefficient. The angle θ between initial wave-vector $\boldsymbol{k}$ and final wave-vector $\boldsymbol{k'}$ for piezoelectric scattering is given by the following equation[89]

$$cos\theta = 1 + \frac{\hbar^2q_D^2}{4m^*\gamma(E)}\left[1-\left(1+\frac{8m^*\gamma(E)}{\hbar^2q_D^2}\right)^r\right] \tag{14}$$

where r in a uniformly distributed random number between 0 and 1.

Acoustic Phonon Scattering

Acoustic phonon scattering occurs due to scattering of electrons by non-polar acoustic phonons. Such scattering is also treated using elastic and equipartition approximation. The scattering rate for this process is given by[79,82]

$$W(E) = \frac{\sqrt{2}m^{*^{3/2}}k_BTD_{ac}^2}{\pi\hbar^4\rho v_s^2}\sqrt{E(1+\alpha E)}(1+2\alpha E) \tag{15}$$

where D_{ac} is acoustic deformation potential, ρ is density of material and v_s is sound velocity. The angle θ between initial wave-vector $\boldsymbol{k}$ and final wave-vector $\boldsymbol{k'}$ for acoustic phonon scattering is given by the following probability distribution function[84,85]

$$P(cos\theta)d(cos\theta) = a_{ac}\{1+\alpha E(1+cos\theta)\}^2d(cos\theta) \tag{16}$$

where a_{ac} is a normalization constant. The random values of $cos\theta$ with the above probability distribution is obtained by using von Neumann rejection.[84,86]

Alloy Scattering

There is an additional scattering mechanism in semiconductor alloys of free carriers due to random fluctuations in the perfect periodicity of the crystal. The alloy scattering rate for electrons is given by[90–92]

$$W(E) = \frac{3\pi}{8\sqrt{2}}\frac{m^{*\frac{3}{2}}}{\hbar^4}x(1-x)V_0U_{all}^2(1+2\alpha E)S(E)\sqrt{E(1+\alpha E)} \tag{17}$$

where x is the mole fraction, V_0 is the primitive cell volume and U_{all} is alloy scattering potential. We have taken a value of 0.47 eV for alloy scattering potential.[93] Here, $S(E)$ is an energy-dependent parameter that describe the effect of alloy ordering on the scattering rate. The value of $S(E)$ lies between 0 and 1. $S(E) = 0$ refers to perfectly ordered alloy system and $S(E) = 1$ refers to a completely random alloy system. Throughout the simulation, $S = 1$ is considered. Alloy scattering is an isotropic scattering mechanism and it is treated by using elastic approximation.

Intervalley Phonon Scattering

The scattering rate due to intervalley phonons is given by[79,82]

$$W(E) = \frac{\pi D_i^2 Z}{\rho \omega_i}\left(\frac{(2m^*)^{\frac{3}{2}}\sqrt{E'(1+\alpha E')}(1+2\alpha E')}{4\pi^2\hbar^3}\right) \times \begin{Bmatrix} N(\omega_i) & (absorption) \\ (N(\omega_i)+1) & (emission) \end{Bmatrix} \tag{18}$$

where $E' = E + \hbar\omega_i - \triangle E$ for absorption and $E' = E - \hbar\omega_i - \triangle E$ for emission of intervalley phonon, if $E' < 0$ intervalley scattering will not occur. For intravalley scattering $\triangle E = 0$ and for intervalley scattering $\triangle E$ is the difference between bottom of energy band between two valleys. D_i is intervalley scattering coupling constant, Z is the number of final valley for intervalley scattering, $N(\omega_i)$ is the number of phonons involved in the transition, ω_i is intervalley phonon frequency. $N(\omega_i)$ is given by

$$N(\omega_i) = \frac{1}{e^{\frac{\hbar\omega_i}{k_B T}} - 1} \tag{19}$$

Intervalley scattering is considered here to be isotropic in nature. Hence, final states after intervalley are equally probable, restricted to only conservation of energy.

Impact Ionization Scattering

The scattering rate due to impact ionization is treated by using the Keldysh expression[94]

$$\frac{1}{\tau_{ii}(E)} = \begin{Bmatrix} 0 & E < E_{th} \\ \frac{P}{\tau(E_{th})}\left(\frac{E-E_{th}}{E_{th}}\right)^2 & E > E_{th} \end{Bmatrix}. \tag{20}$$

where $\frac{1}{\tau_{ii}(E)}$ is the impact ionization scattering rate for an electron. $\frac{1}{\tau(E_{th})}$ is the scattering rate at the threshold energy E_{th} and P is a dimensionless coupling constant. In our simulation, threshold energy E_{th} and P are treated as fitting parameters.

The angle θ between initial wave-vector $\boldsymbol{k}$ and final wave-vector $\boldsymbol{k}'$ for impact ionization scattering is given by the following equation[95]

$$cos\theta = -\frac{1 + G(1-2r)}{2r - (G+3)} \tag{21}$$

where

$$G = \frac{k^2 + k'^2 + \gamma^2}{kk'} \tag{22}$$

For all scattering mechanisms, the azimuthal angle ϕ is completely random, and hence ϕ can be easily calculated using a uniformly distributed random number r between 0 and 1, with $\phi = 2\pi r$. The magnitude of the final state wave-vector $\boldsymbol{k}'$, is determined by using the energy conservation for any given scattering mechanism.

Diffusion

The diffusion constant is an important parameter to understand carrier transport in semiconductors. In the recent past, a lot of work has been done with the Monte Carlo technique for high field diffusivity calculations, especially in small semiconductor devices.[96–99] At a lower field, diffusion D and mobility μ are related by the Einstein relation $D = \frac{\mu k_B T}{e}$. At a higher electric field or in the presence of intervalley scattering, The Einstein relation fails and the diffusion constant cannot be calculated by applying it. In the present work, the following equation is used to calculate the diffusion constant along the longitudinal direction[98,100]

$$D_l = \frac{< (x_l(t) - < x_l(t) >)^2 >}{2t} \tag{23}$$

where $x_l(t)$ is the displacement along the external field direction at time t, and the brackets $< ... >$ denote the ensemble averages. While evaluating with Eq. 23, both ensemble and time averages are taken into account in Monte Carlo simulation. For evaluation of diffusivity along the transverse direction to the field D_t the same expression as 23 is used just by substituting the displacement along the transverse direction instead of the parallel direction in Eq. 23, respectively.

The above Eq. 23 neglects the electron-electron repulsion and assumes that the electric field is constant everywhere and is valid only when macroscopic Fick's law is applicable. Equation 23 is obtained from Fick's law given below,

$$\frac{\partial n}{\partial t} = D_l \frac{\partial^2 n}{\partial x_l^2} - v_d \frac{\partial n}{\partial x_l} \tag{24}$$

Here, n is the electron density and v_d is the drift velocity. Equation 23 is obtained from the second moment of the electron density. For the transient conditions, as Fick's law does not hold, Eq. 23 cannot be employed. For the present study, we report the diffusivity only for the steady-state conditions.

Relaxation Time

The momentum relaxation time τ_m at steady state is calculated by using the following equation[98,101–103]

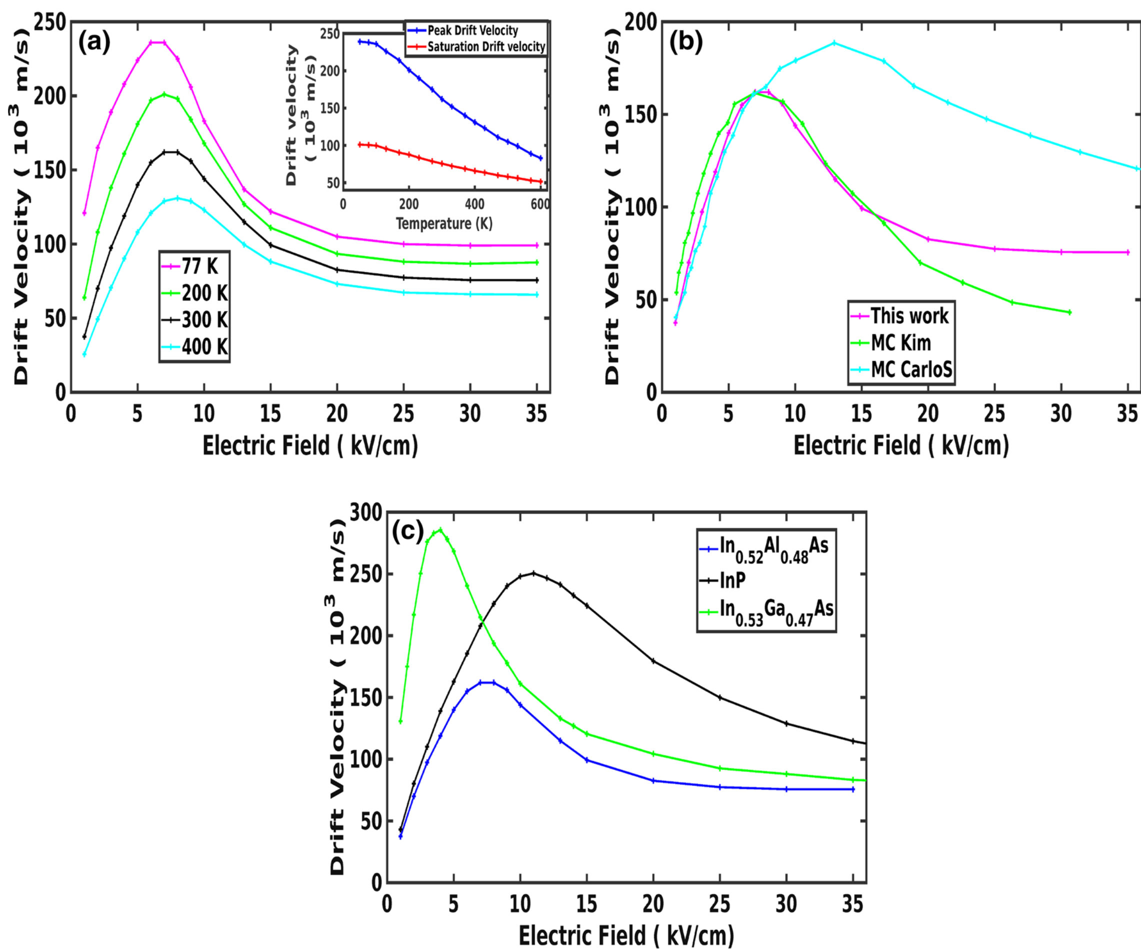

Fig. 1 (a) Drift velocity as a function of applied electric field for n-type $In_{0.52}Al_{0.48}As$ with a doping concentration of $1 \times 10^{22} m^{-3}$ at different crystal temperatures. (b) Drift velocity as a function of applied electric field for n-type $In_{0.52}Al_{0.48}As$ with a doping concentration of $1 \times 10^{22} m^{-3}$ at 300 K. We compared our result with other simulated results Ref.77 and 78. (c) Drift velocity as a function of applied electric field for $In_{0.52}Al_{0.48}As$, InP and $In_{0.53}Ga_{0.47}As$ with a doping concentration of $1 \times 10^{22} m^{-3}$ at 300 K.

$$\tau_m = \frac{m_{eff} v_{ss}}{qF} \tag{25}$$

where m_{eff} is the effective mass over ensemble and is given by $m_{eff} = m^*(1 + 2\alpha E)$. v_{ss} is the steady-state average drift velocity of electrons and F is the applied electric field.

The energy relaxation time τ_e at steady state is calculated by using the following equation[98,101–103]

$$\tau_e = \frac{\overline{E} - \overline{E}_0}{e v_{ss} F} \tag{26}$$

where $\overline{E}$ is the average electron energy in the presence of a field and $\overline{E}_0 = \frac{3}{2} k_B T$ is the thermal energy. The energy relaxation time can give insights into the transient effect of the material. Generally, a higher energy relaxation time leads to higher transient effects.[103,104]

Results and Discussion

Steady-State Electron Transport

In Fig. 1a we show the drift velocity with electric field for different lattice temperatures. At a lower electric field, equilibrium is maintained by polar optical phonon scattering. As the electric field increases, electrons gain more energy. Around the threshold field, polar optical phonon scattering is not able to fully dissipate the energy gained by electrons from the electric field, and electric breakdown occurs if intervalley scattering does not become active.

As the electric field increases, electrons are more effectively accelerated and they gain more energy. Since the effective mass of electron is given by $m^*(1 + 2\alpha E)$, firstly as electron energy increases electron effective mass also increases and secondly, at higher energy intervalley scattering also plays a role and electrons move to a higher energy

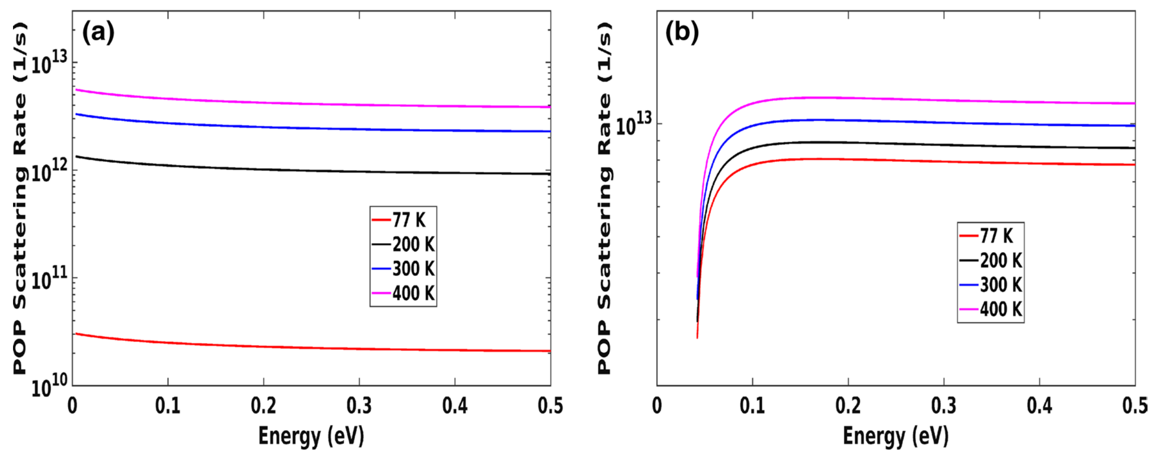

Fig. 2 Polar optical phonon scattering rate as a function of electron energy for different temperatures in the gamma valley due to (a) Absorption of optical phonon (b) Emission of optical phonon for n-type $In_{0.52}Al_{0.48}As$ with a doping concentration of $1 \times 10^{22} m^{-3}$.

L-valley, which also has higher effective mass. After a particular electric field, called threshold or critical electric field, the latter effect becomes more pronounced and the electron velocity starts decreasing. At 300 K $In_{0.52}Al_{0.48}As$ has a peak drift velocity of 1.62×10^5 m/s for an applied electrical field of 7.5 kV/cm at a doping concentration of $1 \times 10^{22} m^{-3}$.

It can be seen that both the peak and the saturation velocity have significant temperature dependence. This can further be noticed from the inset figure in Fig. 1a where peak and saturation drift velocity are plotted with respect to temperature. To understand this temperature dependence, we plot the scattering rates due to the absorption (Fig. 2a) and due to the emission of polar optical phonons (Fig. 2b). As the temperature increases, polar optical phonon scattering rates due to both emission and absorption of polar optical phonons increase, respectively. Similarly, for other scattering mechanisms, scattering rates also increases with the increasing lattice temperature. The increase in phonon scattering rate with temperature causes decrease in peak drift velocity and saturation drift velocity with the increase in crystal temperature.

Figure 1b shows the variation of drift velocity with electric field obtained with in our simulation compared with earlier results obtained by Kim[77] and Dolgos[78]. A good agreement is obtained at a lower electric field with both the earlier theoretical results. Dolgos's simulation shows higher values of peak drift velocity and threshold field than our results. Dolgos used an empirical pseudopotential band structure for the calculation. Since the parameters used for the simulation by Dolgos are not mentioned in the article, the reason for higher values of peak drift velocity and threshold field in Dolgos's simulation remains unclear. But it is probably due to higher energy separation between gamma and L-valley.

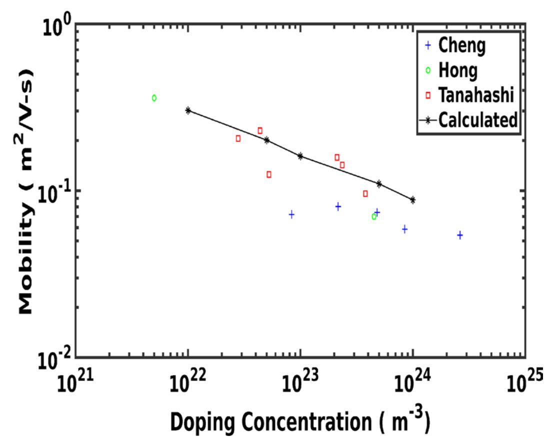

Fig. 3 Mobility as a function doping concentration at 300 K for n-type $In_{0.52}Al_{0.48}As$. Experimental data are included for comparison Ref.105–107.

Figure 1c shows the variation of drift velocity with electric field for a doping concentration of $1 \times 10^{22} m^{-3}$ at 300 K for $In_{0.52}Al_{0.48}As$, InP and $In_{0.53}Ga_{0.47}As$. Material parameters for InP and $In_{0.53}Ga_{0.47}As$ are taken from reference,[108,109] respectively. Both InP and $In_{0.53}Ga_{0.47}As$ have higher peak drift velocity than $In_{0.52}Al_{0.48}As$ due to lower effective mass of electrons in the central gamma valley of InP and $In_{0.53}Ga_{0.47}As$ than $In_{0.52}Al_{0.48}As$. InP has an electron effective mass of $0.08m_0$ and $In_{0.53}Ga_{0.47}As$ has an effective mass of $0.03745m_0$, respectively. InP has a peak drift velocity of 2.50 kV/cm for a critical electric field of 11 kV/cm and $In_{0.53}Ga_{0.47}As$ has a peak drift velocity of 2.85 kV/cm for a critical electric field of 4 kV/cm at 300 K for a doping concentration of $1 \times 10^{22} m^{-3}$.

The electron mobilities are calculated for different doping concentrations at 300 K for n-type $In_{0.52}Al_{0.48}As$ and compared with experimental values of Cheng et al.[105], Hong

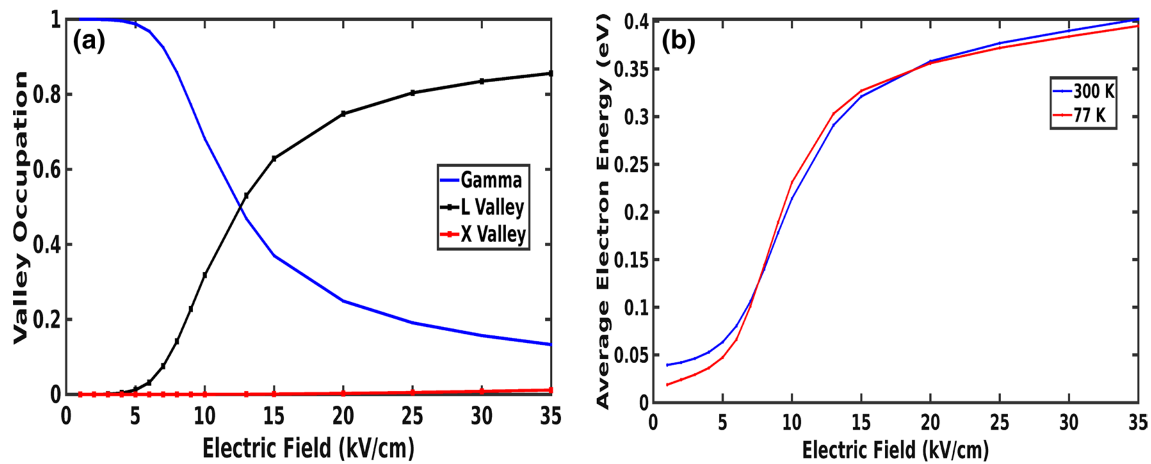

Fig. 4 (a) Relative population in different valleys as a function of electric field at 300 K (b) Average total electron energy as a function of electric field at 77 K and 300 K for n-type $In_{0.52}Al_{0.48}As$ with a doping concentration of $1 \times 10^{22} m^{-3}$.

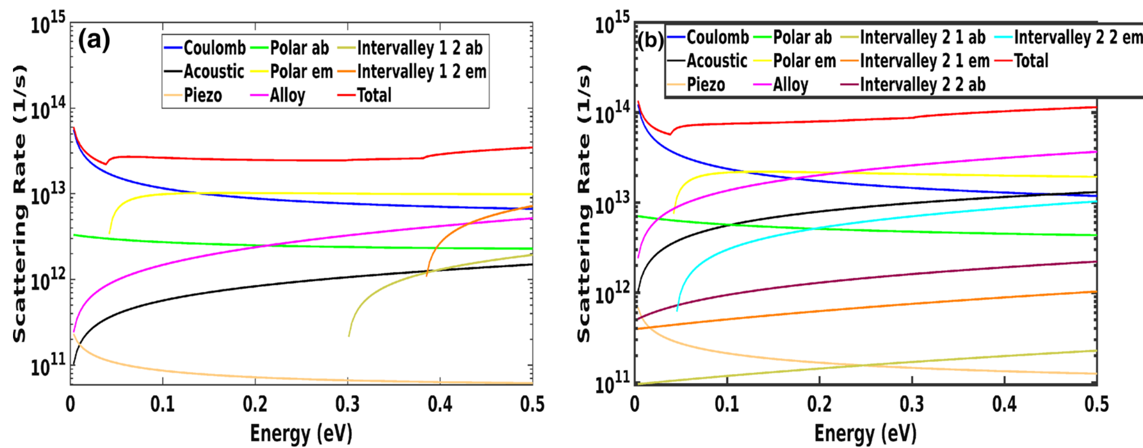

Fig. 5 (a) Scattering rate in the gamma valley as a function of energy (b) Scattering rate in the L-valley as a function of energy for n-type $In_{0.52}Al_{0.48}As$. For both cases temperature is set to 300 K, and a doping concentration of 1×10^{22} m^{-3}.

et al.[106] and Tanahashi et al.[107] as shown in Fig. 3. Cheng et al.[105] and Hong et. al.[106] fabricated the $In_{0.52}Al_{0.48}As$ by using molecular beam epitaxy, and Tanahashi et al.[107] used liquid phase epitaxy. In all three experiments, mobility was calculated by using Hall measurement. In our simulation, mobility is calculated by the ratio of drift velocity to the electric field in the linear region at different values of electric field and then the average value is taken for comparison. Calculated mobilities are in good agreement with experimental reported values. The mobility decreases with the increasing doping concentration due to increased ionized impurity scattering rate at higher doping concentration.

Figure 4a shows the relative population of electrons in different valley as a function of the electric field at 300 K. Valley occupancy of electrons in the X-valley remains smaller for all ranges of applied field strength. Around a threshold field 7.5 kV/cm there is a significant increase of electron occupancy in the L-valley with the increase of electric field, and simultaneously, the drift velocity of electrons starts decreasing due to higher effective mass of electrons in the L-valley than gamma valley electrons. So negative differential velocity in the $In_{0.52}Al_{0.48}As$ is due to intervalley transfer of electrons to a higher L-valley.

Figure 4b shows the average total electron energy as a function of electric field at 77 K and 300 K. Near the threshold field, most of the electrons are in the gamma valley and polar optical phonon scattering by emission of phonons is the most dominant scattering mechanism. It relaxes electron energy by only 0.0397 eV, while at a higher electric field above 20 kV/cm, most of the electrons are shifted to a higher valley and intervalley scattering becomes the dominant scattering mechanism. Polar optical scattering in the L-valley also has a higher scattering rate than polar optical phonon scattering of the gamma valley. So, due to the lower

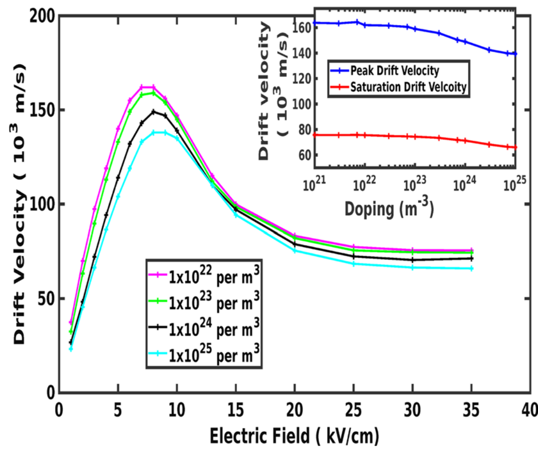

Fig. 6 Drift velocity as a function of applied electric field for different doping concentrations at 300 K for n-type $In_{0.52}Al_{0.48}As$. The inset Fig. shows the variation of peak drift velocity and saturation drift velocity with doping concentration at 300 K for n-type $In_{0.52}Al_{0.48}As$.

scattering rate in the gamma valley, electron energy shows a sharp upward turn near the threshold field, while at a higher field due to the higher scattering rate in the L-valley, it shows small variation with the electric field.

In Fig. 5a, the scattering rate for different scattering mechanisms and total scattering rate except impact ionization scattering rate as a function of electron energy are plotted for the central gamma valley at 300 K. At low electron energy ionized impurity scattering is the most dominant scattering and above approximately 0.14 eV polar optical phonon scattering by emission of phonons is the most dominant scattering mechanism.

In Fig. 5b the scattering rate for different scattering mechanisms and total scattering rate as a function of energy are plotted for the L-valley at 300 K. Since most of the electrons remain in gamma and L-valleys for the electric field of interest, the intervalley scattering of carriers to the X-valley is not shown for convenience in Fig. 5a and b, but it is included in our simulation. The total scattering rate in the L-valley is higher than the total scattering rate in the gamma valley,

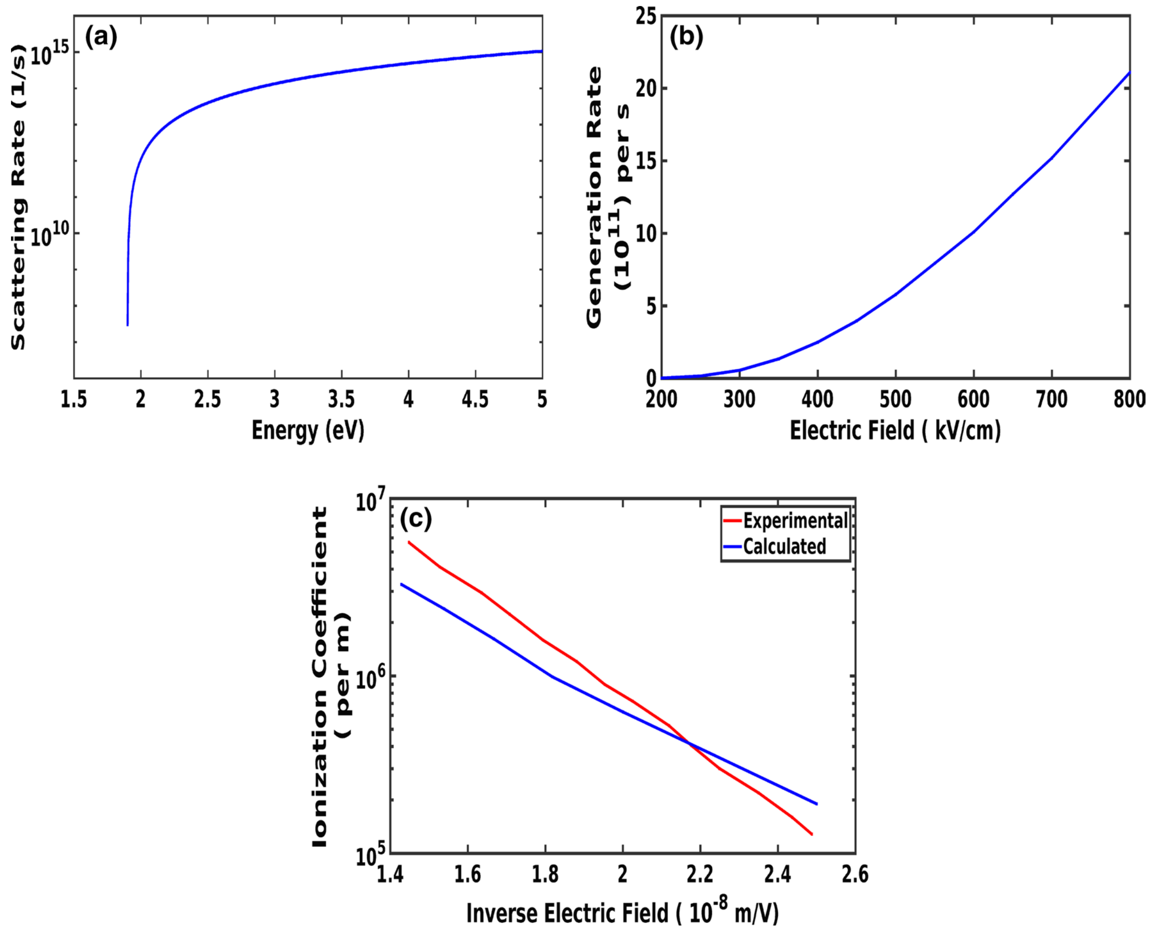

Fig. 7 (a) Impact ionization scattering rate in gamma valley as a function of energy. (b) Impact ionization generation rate as a function of applied electric field (c) Impact ionization coefficient as a function of inverse of the applied electric field for n-type $In_{0.52}Al_{0.48}As$. Experimental curve is taken from Ref.[110]. For all cases doping concentration is set to $2 \times 10^{22} m^{-3}$ and crystal temperature is 298 K.

due to the higher effective mass of electrons there, since first-order approximation scattering rates are considered to be proportional to the density of states and for non-parabolic bands. The density of states is given by

$$g(E) = \frac{(2m^*)^{\frac{3}{2}}\sqrt{E(1+\alpha E)}(1+2\alpha E)}{4\pi^2\hbar^3} \quad (27)$$

Figure 6 shows the variation of drift velocity with electric field for different doping concentrations. As doping concentration increases, drift velocity, peak velocity and low field mobility are reduced and the threshold field is shifted to higher electric field values. With the increase in doping concentration, ionized impurity scattering rate increases as the ionized impurity scattering rate is directly proportional to doping concentration, hence, drift velocity and peak velocity decrease. Higher ionized impurity scattering rate at higher doping concentration causes lower electron energy and increases the electric field needed to reach peak drift velocity. From Fig. 5a it is clear that at lower electron energy ionized impurity scattering is the most dominant scattering mechanism, while at higher electron energy, ionized impurity scattering is not so significant. Our simulation results in Fig. 6 also depicts the same. At a lower field, ionized impurity scattering has a significant effect, while at higher electric field saturation velocity, is not significantly affected by doping concentration variation.

Table III Parameters for impact ionization

Parameter	$E_{th}(eV)$	P
First conduction band	1.9	4×10^{14}
Second conduction band	2.3	1×10^{15}
Third conduction band	2.4	1×10^{16}

Figure 7a shows the scattering rate due to impact ionization scattering. The threshold energy of impact ionization in the gamma valley is 1.9 eV, so impact ionization becomes active only after 1.9 eV energy in the gamma valley. Figure 7b shows the variation of the generation rate due to impact ionization with electric field obtained in our simulation for a doping concentration of $2\times10^{22}m^{-3}$ at 298 K. For impact ionization threshold energy E_{th} and P are treated as fitting parameters, and their values we have obtained are written in Table III for different conduction bands. Figure 7c shows the variation of impact ionization coefficient with the inverse of electric field. Theoretical obtained values are compared with the experimental values of Watanabe.[110] Impact ionization rates in $In_{0.52}Al_{0.48}As$ were determined by photo-multiplication measurements by Watanabe. A good agreement between the experimental[110] and theoretical curve for impact ionization coefficient is obtained. Calculated ionization coefficient supports the theory of Shockley.[111] According to Shockley's theory, the impact ionization coefficient depends on the electric field as

$$\alpha_{im} \sim exp(-\frac{B}{F}) \quad (28)$$

where B is a constant. B is determined from the simulation to be 2.75×10^8 V/m.

Momentum and Energy Relaxation Time

Figure 8a shows the variation of electron effective mass with electric field. With increasing electric field, average electron energy increases, and electrons are shifted to a higher energy region in the same valley or to the satellite L-valley from the gamma valley. Both of these factors lead to an increase in electron effective mass, since the electron effective mass is given by $m_{eff} = m^*(1+2\alpha E)$; therefore, with increasing

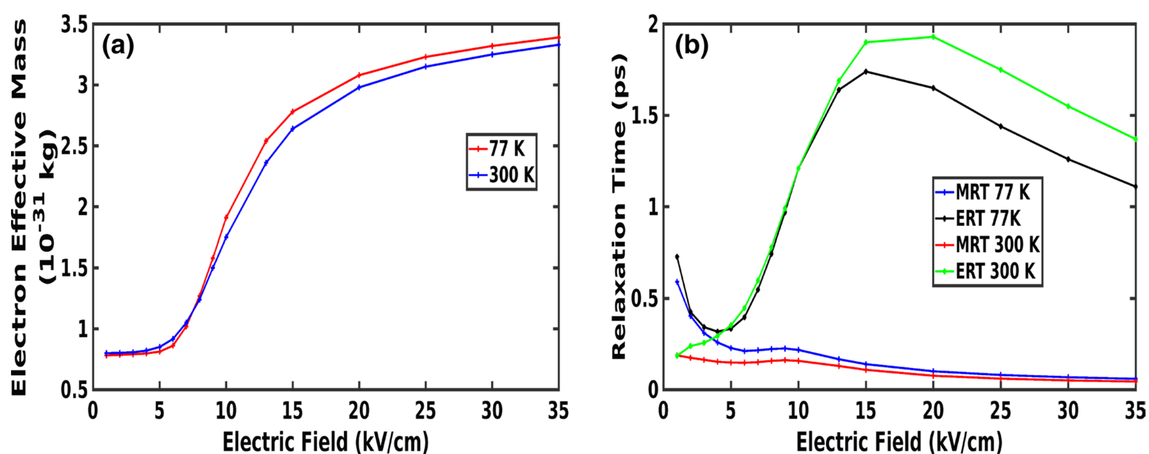

Fig. 8 (a) Electron effective mass as a function of electric field at 77 K and 300 K (b) Momentum and energy relaxation time as a function of electric field at 77 K and 300 K for n-type $In_{0.52}Al_{0.48}As$ with a doping concentration of $1\times10^{22}m^{-3}$.

electric field, electrons are shifted to a higher energy region in the same valley. Hence, their effective mass also increases, and if electrons are shifted to the L-valley, then the L-valley also has a higher effective mass than the gamma valley. In the low field region, electron effective mass remains almost fixed with increasing electric field. Between regions of 5 kV/cm to 25 kV/cm electrical field, there is a significant increase in electron effective mass with increasing electric field, since due to inter-valley scattering many electrons are shifted to the L-valley from the gamma valley in this region. At higher electric field after 25 kV/cm, there is a very slow increase in electron effective mass, since, as also depicted in Fig. 4a, after 25 kV/cm there is a slight increase in L-valley occupancy.

Figure 8b shows the variation of momentum and energy relaxation time with electric field at 77 K and 300 K. Momentum relaxation time decreases with increasing electric field. At a lower electric field most of the electrons are in the gamma valley, and intervalley scattering will not play the main role. In the absence of intervalley scattering at a lower electric field, electrons decrease momentum over longer time and result in higher momentum relaxation time. At higher electric field intervalley scattering, the scattering becomes important and electron momentum decreases at a faster rate due to higher effective mass and the higher scattering rate in the upper valley.

At 300 K in the low field region between 1 kV/cm to 20 kV/cm, energy relaxation time increases with electric field and then start decreasing with electric field. In the low field region between 5 kV/cm to 20 kV/cm as show in Fig. 4b, average electron energy increases with electric field significantly and later increases at a slower rate. In the lower field region, most of the electrons are in the gamma valley and energy is relaxed by mainly emitting polar optical phonons. However, less energy of electrons is released by emitting polar optical phonons in this region, resulting in a sharp increase of average electron energy and energy relaxation time. At a higher electric field, intervalley scattering will begin to play an important role, and at a higher electric field most of the electrons are occupied in the higher L-valley, which has a much higher total scattering rate than the gamma valley total scattering rate, so energy relaxation time starts decreasing at higher electric field.

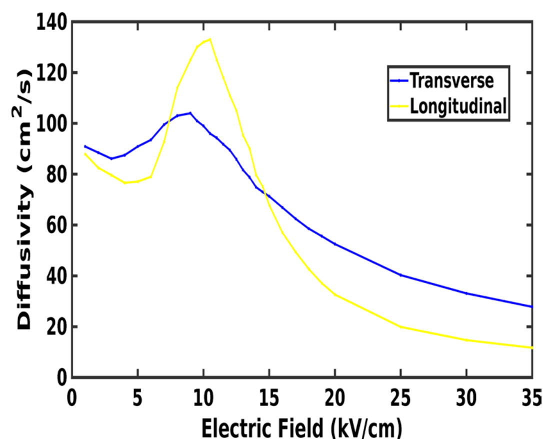

Fig. 9 Diffusivity as a function of electric field at 300 K for n-type $In_{0.52}Al_{0.48}As$ with a doping concentration of $1 \times 10^{22} m^{-3}$.

Diffusion Coefficient

Figure 9 shows the variation of longitudinal and transverse diffusion coefficient with electric field at 300 K. Both longitudinal and transverse diffusion coefficients show a peak in diffusivity near the critical electrical field. Below or around the critical electrical field due to rapid increase in electron energy raises the diffusion coefficient. At significantly high electric fields above critical field, average electron energy increases slowly and drift velocity and mobility reduces, further due to intervalley scattering, electrons are shifted to higher effective mass satellite valley. Hence, at higher electric field, diffusion coefficient reduces to very low values. Saturated drift velocity and low diffusion coefficient at higher electric field may have remarkable implications for high frequency device operations. The smaller values of longitudinal and transverse diffusion coefficient at higher electric field lead to lower diffusion noise. So, lower diffusion noise can be achieved by applying the higher electric fields without loss of speed. The anisotropy between longitudinal and transfer diffusion coefficient in $In_{0.52}Al_{0.48}As$ is lower than observed in InP[112] and CdTe,[113] and of approximately same magnitude as GaAs.[84] This reflects a lower energy separation between central and satellite valley of $In_{0.52}Al_{0.48}As$ (0.34 eV) than InP (0.52 eV)and CdTe (1.5 eV) and of approximately same magnitude as of GaAs (0.35 eV) and it supports the explanation of the difference between the two coefficients given in Refs. 113, 84.

Transient Electron Transport

We now examine the transient electron transport of $In_{0.52}Al_{0.48}As$. Figure 10a shows the electron drift velocity as a function of the distance traveled upon the application of electric field for various applied electric field strength at 300 K. For an applied field up to 7.5 kV/cm, the electron reaches steady state very quickly with little or no velocity overshoot. For an applied electric field higher than 7.5 kV/cm significant velocity overshoot occurs. This result suggests that for $In_{0.52}Al_{0.48}As$ 7.5 kV/cm is the critical applied field strength for the onset of velocity overshoot effects. At 300 K it is already mentioned that 7.5 kV/cm corresponds to the electric field for peak drift velocity. For GaN, ZnO and

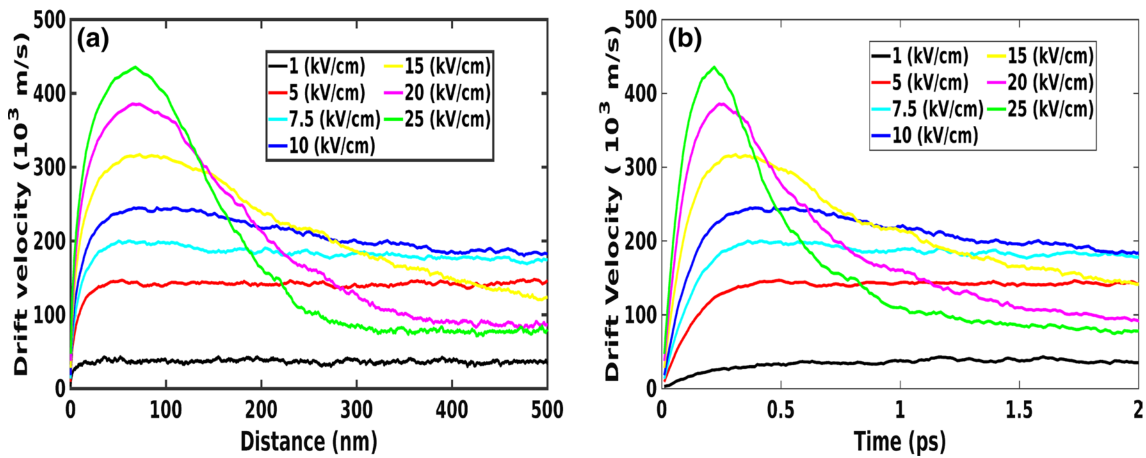

Fig. 10 (a) Drift velocity as a function of distance displaced, for various applied electric field strength. (b) Drift velocity as a function of time elapsed since the application of electric field, for various applied electric field strength for n-type $In_{0.52}Al_{0.48}As$. For all cases the temperature is set to 300 K and doping concentration of $1 \times 10^{22} m^{-3}$.

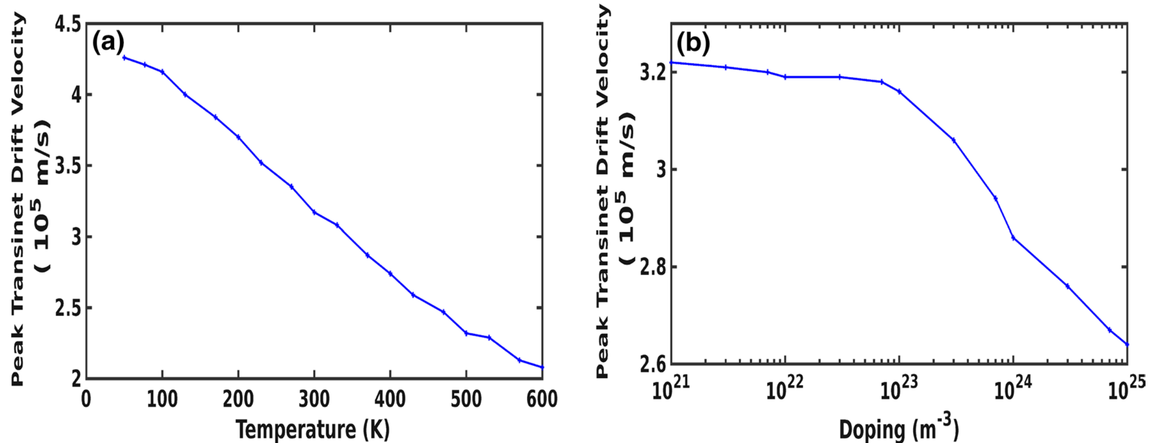

Fig. 11 (a) Peak transient drift velocity as a function of temperature with a doping concentration of $1 \times 10^{22} m^{-3}$ for n-type $In_{0.52}Al_{0.48}As$. (b) Peak transient drift velocity as a function of doping concentration for n-type $In_{0.52}Al_{0.48}As$ at 300 K. For both cases the applied electric field strength is set to 15 kV/cm.

other III-V semiconductors as well, a little velocity overshoot is observed and electron reaches steady state very quickly below the critical electrical field.[114,115]

Figure 10b shows the drift velocity variation with time. It has also the same trend as Fig. 10a. For up to 7.5 kV/cm electric field, there is very little or no overshoot. For an electric field higher than 7.5 kV/cm there is significant velocity overshoot. Figure 11a shows the variation of peak transient drift velocity as function of temperature, and Fig. 11b shows the variation of peak transient drift velocity with doping concentration. For both cases the applied electric field strength being set to 15 kV/cm. Peak transient drift velocity decreases with the increasing temperature and doping concentration. At higher temperatures, increase in phonon scattering rate causes decreases in peak transient drift velocity, and at higher doping concentration increased ionized impurity scattering rate reduces peak transient drift velocity.

Figure 12 shows the variation of drift velocity with distance for different temperatures. We have followed the same approach as in the paper[114] and set the electric field to twice the approximate critical field for each case. The critical field for temperatures 77 K, 200 K, 300 K and 400 K are 6 kV/cm, 7 kV/cm, 7.5 kV/cm and 8 kV/cm, respectively. Crystal temperature has a significant effect on transient electron transport. Peak drift velocity is about 371 m/s when the temperature is 77 K and it decreases to about 281 m/s when the crystal temperature is about 400 K. For higher crystal temperatures, steady state is achieved at a much higher rate.

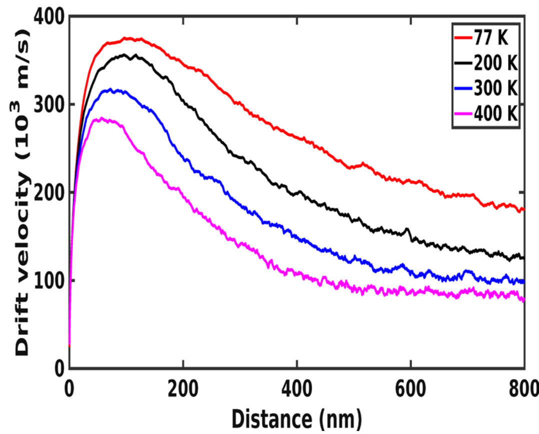

Fig. 12 Electron drift velocity as a function of distance displaced since the application of electric field at different temperatures for n-type $In_{0.52}Al_{0.48}As$ with a doping concentration of $1 \times 10^{22} m^{-3}$. For all cases the electric field is set to two times the critical electric field.

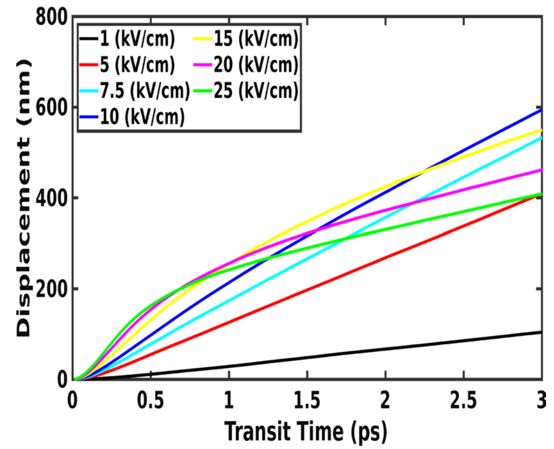

Fig. 14 Electron displacement as a function of transit time for various applied field strength at 300 K for n-type $In_{0.52}Al_{0.48}As$ with a doping concentration of $1 \times 10^{22} m^{-3}$.

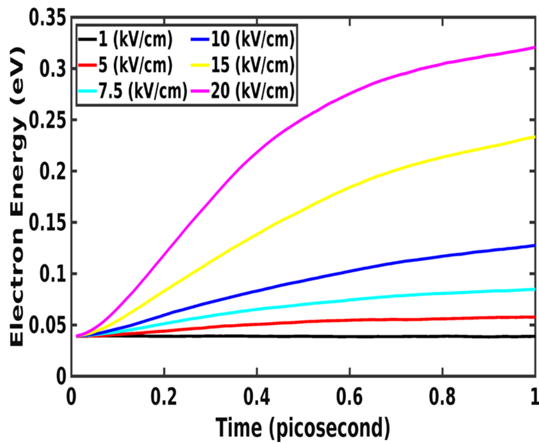

Fig. 13 Electron energy as a function of time elapsed since the application of electric field, for various applied electric field strengths for n-type $In_{0.52}Al_{0.48}As$. For all cases the temperature is set to 300 K and doping concentration of $1 \times 10^{22} m^{-3}$.

Figure 13 shows the variation of electron energy with time for different applied electric fields at 300 K. Electron energy increases monotonically with time for all applied electric fields until it reaches steady state. For a low applied electric field steady state is reached very quickly.

Figure 14 shows the variation of electron displacement as a function of time elapsed since the application of electric field for a number of different cases. Electron displacement increases monotonically in response to an increase in time elapsed since the onset of applied electric field. Figure 15a, b and c shows the variation of transit time as a function of distance traveled for $In_{0.52}Al_{0.48}As$, InP and $In_{0.53}Ga_{0.47}As$ for 100 nm, 300 nm and 1000 nm device lengths. The applied electric field are chosen to minimize the electron transit time across the shown device lengths.

In $In_{0.53}Ga_{0.47}As$ and InP electron travels at faster rate than $In_{0.52}Al_{0.48}As$ due to the lower effective mass of electrons in the gamma valley. The upper bound on the cut-off frequency of a device is given by the formula

$$f_T = \frac{1}{2\pi\tau} \quad (29)$$

where τ is transit time across the device. We calculated the upper bound on cut-off frequency at 100 nm device length for $In_{0.52}Al_{0.48}As$ to be 663 GHz, for InP to be 791 GHz and for $In_{0.53}Ga_{0.47}As$ to be 1.53 THz.

Device Implications

The transient electron transport that we have studied here can be related to the performance of electron device fabricated from $In_{0.52}Al_{0.48}As$. To determine an upper bound for cut-off frequency, first we have to determine the minimum transit time occurring for optimally chosen applied field. In Fig. 16 we have plotted the average transit time as a function of displacement for different applied electric fields. In this curve for a displacement of 300 nm, minimum transit time is obtained with an electric field of 15 kV/cm. Similarly, we have calculated the minimum transit time required for different device lengths of $In_{0.52}Al_{0.48}As$ material. From this optimization procedure, we have calculated the upper bound on the cut-off frequency for different device lengths and plotted the results in Fig. 17. The blue curve in Fig. 17 represents the optimized results obtained by incorporating the velocity overshot effect occurring during the transient state of electron transport, while the red curve in Fig. 17 represents the upper bound on cut-off frequency obtained by applying the field which produces largest steady state

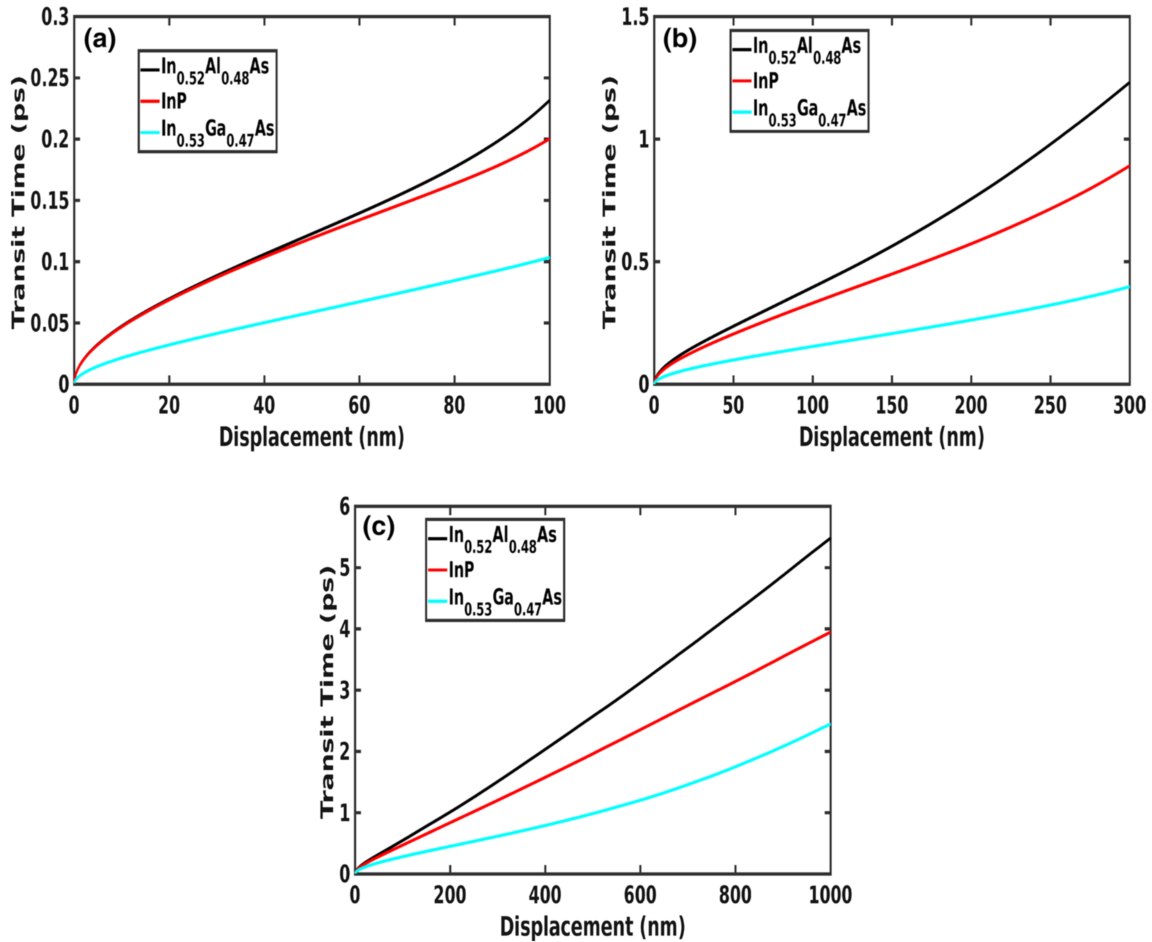

Fig. 15 Electron transit time as a function of distance for n-type $In_{0.52}Al_{0.48}As$, InP and $In_{0.53}Ga_{0.47}As$. For all cases temperature is set to 300 K and doping concentration of $1 \times 10^{22} m^{-3}$. The field strengths are chosen to minimize the transit time across the device lengths. (a) For 100 nm device length. The applied fields are 51 kV/cm for $In_{0.52}Al_{0.48}As$, 50 kV/cm for InP and 120 kV/cm for $In_{0.53}Ga_{0.47}As$. (b) For 300 nm device length. The applied fields are 15 kV/cm for $In_{0.52}Al_{0.48}As$, 18 kV/cm for InP and 32 kV/cm for $In_{0.53}Ga_{0.47}As$. (c) For 1000 nm device length. The applied fields are 9 kV/cm for $In_{0.52}Al_{0.48}As$, 10 kV/cm for InP and 9 kV/cm for $In_{0.53}Ga_{0.47}As$.

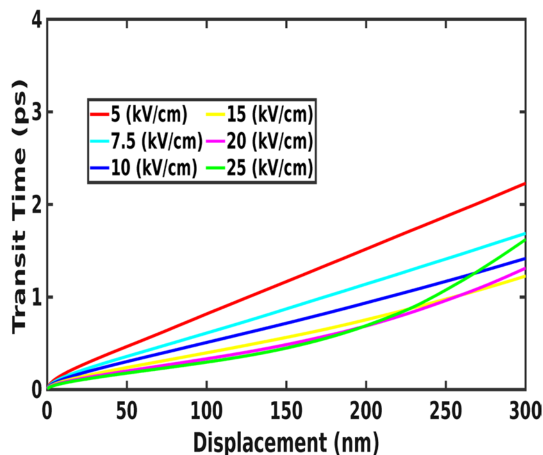

Fig. 16 Electron transit time as a function of distance displaced for various applied electric field strength at 300 K for n-type $In_{0.52}Al_{0.48}As$ with a doping concentration of $1 \times 10^{22} m^{-3}$.

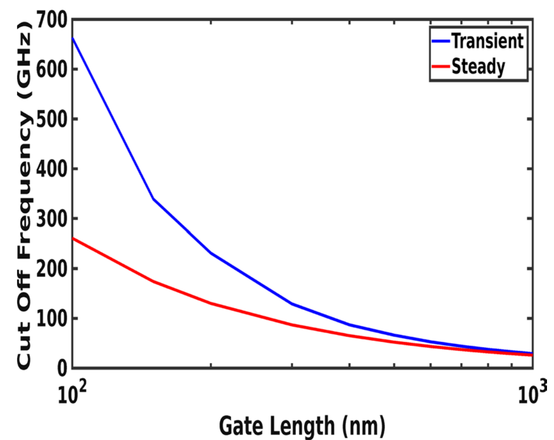

Fig. 17 The optimal cut-off frequency as a function of device gate length. The blue curve is obtained by including velocity overshoot effect and the red curve is obtained without including velocity overshoot effect for n-type $In_{0.52}Al_{0.48}As$ at 300 K with a doping concentration of $1 \times 10^{22} m^{-3}$.

electron velocity, i.e. this curve does not include the effect of transient state. At a shorter device length there is significant improvement in the upper bound on the cut-off frequency obtained due to velocity overshoot effect. For device lengths less than 700 nm, transient effect becomes noticeable and it becomes more pronounced as device length is diminished further. For a device length of 100 nm, the upper bound on cut-off frequency is improved from 261 GHz to 663 GHz by including the transient effect in the calculation. For 100 nm length minimum transient is obtained by applying an electric field of 51 kV/cm. For a device length of 100 nm an upper bound cut-off frequency of 637 GHz and 1.05 THz is reported for GaAs and ZnO,[116] respectively. We conclude that $In_{0.52}Al_{0.48}As$ based devices have equal or higher frequency capability than GaAs based devices when transit time is an important factor. While doing the calculation of upper bound on cut-off frequency, all non-idealities occurring during normal device operation are ignored.

Conclusion

We presented a detailed and comprehensive study of steady-state and transient electronic transport in $In_{0.52}Al_{0.48}As$ with the three-valley model, using the semi-classical ensemble Monte Carlo method and including all important scattering mechanisms. All electronic transport parameters such as drift velocity, valley occupation, average electron energy, ionization coefficient and generation rate, electron effective mass, diffusion coefficient, energy and momentum relaxation time were extracted rigorously from the simulations. Using these, we presented a detailed characterization of the transient electronic transport showing the variation of drift velocity with distance and time. If the applied electric field is higher than a threshold field 7.5 kV/cm for peak drift velocity, the velocity overshoot is shown to occur in a transient state. Transient effects become more pronounced at shorter device length scales. We then estimated the optimal cut-off frequencies for various device lengths via the velocity overshoot effect. Our analysis showed that for device lengths shorter than 700 nm, transient effects are significant and should be taken into account for optimal device designs. As a critical example, at length scales of around 100 nm, we obtained a significant improvement in the cut-off frequency from 261 GHz to 663 GHz with the inclusion of transient effects. The field dependence of all extracted parameters here could prove to be helpful for further device analysis and design.

Acknowledgments AKM and BM gratefully acknowledge funding from Indo-Korea Science and Technology Center (IKST), Bangalore.

Conflict of interest The authors declare that they have no conflict of interest.

References

1. J. Jogi, S. Sen, M. Gupta, R. Gupta, Microw. Opt. Technol. Lett. 29, 66 (2001)
2. J. Jogi, S. Pandey, R. Gupta, in *Microwave and Optical Technology 2003* (International Society for Optics and Photonics, 2004), vol. 5445, pp. 290–293.
3. Y. Xie, in Topical Workshop on Heterostructure Microelectronics, Kyoto. Jpn. Abst. 2000, 24–25 (2000)
4. N.C. Paul, K. Nakamura, H. Seto, K. Iiyama, S. Takamiya, Jpn. J. Appl. Phys. 44, 1174 (2005)
5. U. Mishra, A. Brown, L. Jelloian, M. Thompson, L. Nguyen, S. Rosenbaum, in *International Technical Digest on Electron Devices Meeting* (IEEE, 1989), pp. 101–104.
6. L.D. Nguyen, A.S. Brown, M.A. Thompson, L.M. Jelloian, IEEE Trans. Electron. Devices 39, 2007 (1992)
7. T. Enoki, K. Arai, Y. Ishii, IEEE Electron. Device Lett. 11, 502 (1990)
8. Y. Yamashita, A. Endoh, K. Shinohara, M. Higashiwaki, K. Hikosaka, T. Mimura, S. Hiyamizu, T. Matsui, IEEE Electron. Device Lett. 22, 367 (2001)
9. P. Ho, M. Kao, P. Chao, K. Duh, J. Ballingall, S. Allen, A. Tessmer, P. Smith, Electron. Lett. 27, 325 (1991)
10. L. Nguyen, L. Jelloian, M. Thompson, M. Lui, in *International Technical Digest on Electron Devices* (IEEE, 1990), pp. 499–502.
11. D. Streit, K. Tan, R. Dia, A. Han, P. Liu, H. Yen, P. Chow, Electron. Lett. 27, 1149 (1991)
12. D. Welch, G. Wicks, L. Eastman, J. Appl. Phys. 55, 3176 (1984)
13. U. Mishra, A. Brown, L. Jelloian, L. Hackett, M. Delaney, IEEE Electron. Device Lett. 9, 41 (1988)
14. G.-G. Zhou, A. Fischer-Colbrie, J. Miller, Y.-C. Pao, B. Hughes, L. Studebaker, J. Harris, in *International Electron Devices Meeting 1991 [Technical Digest]* (IEEE, 1991), pp. 247–250.
15. J. Ajayan, D. Nirmal, Superlatt. Microstruct. 86, 1 (2015)
16. S. Luryi, P.M. Mensz, M.R. Pinto, P.A. Garbinski, A.Y. Cho, D.L. Sivco, Appl. Phys. Lett. 57, 1787 (1990)
17. H. Temkin, K. Alavi, W. Wagner, T. Pearsall, A. Cho, Appl. Phys. Lett. 42, 845 (1983)
18. R. Lai, X. Mei, S. Sarkozy, W. Yoshida, P. Liu, J. Lee, M. Lange, V. Radisic, K. Leong, W. Deal, in *2010 22nd International Conference on Indium Phosphide and Related Materials (IPRM)* (IEEE, 2010), pp. 1–3.
19. S.-J. Yeon, M. Park, J. Choi, K. Seo, in *2007 IEEE International Electron Devices Meeting* (IEEE, 2007), pp. 613–616.
20. J. Schleeh, G. Alestig, J. Halonen, A. Malmros, B. Nilsson, P. Nilsson, J.P. Starski, N. Wadefalk, H. Zirath, J. Grahn, IEEE Electron. Device Lett. 33, 664 (2012a)
21. D.-H. Kim, J.A. Del Alamo, J.-H. Lee, K.-S. Seo, IEEE Trans. Electron. Devices 54, 2606 (2007)
22. H. Fukui, IEEE Trans. Electron Devices 26, 1032 (1979)
23. Y. Chou, R. Grundbacher, D. Leung, R. Lai, Q. Kan, D. Eng, P. Liu, T. Block, A. Oki, in *International Conference on Indium Phosphide and Related Materials, 2005* (IEEE, 2005), pp. 223–226.
24. W. Deal, X. Mei, K.M. Leong, V. Radisic, S. Sarkozy, R. Lai, IEEE Trans. Terahertz Sci. Technol. 1, 25 (2011)
25. D.-H. Kim, J.A. del Alamo, IEEE Electron. Device Lett. 31, 806 (2010)

26. J. Schleeh, H. Rodilla, N. Wadefalk, P.-Å. Nilsson, J. Grahn, IEEE Trans. Electron. Devices 60, 206 (2012b)
27. M. Pospieszalski, W. Lakatosh, R. Lai, K. Tan, D. Streit, P. Liu, R. Dia, J. Velebir, in *1993 IEEE MTT-S International Microwave Symposium Digest* (IEEE, 1993), pp. 515–518.
28. H. Matsuzaki, T. Maruyama, T. Koasugi, H. Takahashi, M. Tokumitsu, T. Enoki, IEEE Trans. Electron Devices 54, 378 (2007)
29. G. Galiev, I. Vasil'evskii, E. Klimov, A. Klochkov, D. Lavruhin, S. Pushkarev, P. Maltsev, Semiconductors 49, 234 (2015)
30. D. Xu, H.G. Heiß, S.A. Kraus, M. Sexl, G. Bohm, G. Trankle, G. Weimann, G. Abstreiter, IEEE Trans. Electron. Devices 45, 21 (1998)
31. D. Xu, H. Heiss, S. Kraus, M. Sexl, G. Bohm, G. Trankle, G. Weimann, G. Abstreiter, IEEE Electron. Device Lett. 18, 323 (1997)
32. R. Ranjani, R. Vaishnavi, N. Mohankumar, A. Mohanbabu, in *2017 Devices for Integrated Circuit (DevIC)* (IEEE, 2017), pp. 702–707.
33. C. Wang, Y. Lin, C. Kuo, M. Lee, J. Yao, T. Huang, H. Hsu, E. Y. Chang, in *2019 14th European Microwave Integrated Circuits Conference (EuMIC)* (IEEE, 2019), pp. 204–207.
34. M. Kawano, T. Kuzuhara, H. Kawasaki, F. Sasaki, H. Tokuda, IEEE Microw. Guided Wave Lett. 7, 6 (1997)
35. M. Chertouk, H. Heiss, D. Xu, S. Kraus, W. Klein, G. Bohm, G. Trankle, G. Weimann, IEEE Electron. Device Lett. 17, 273 (1996)
36. W. Hänsch, *The Drift Diffusion Equation and its Applications in MOSFET Modeling* (Springer Science, 2012).
37. M. Rudan, F. Odeh, COMPEL-Int. J. Comput. Math. Electr. Electron. Eng. (1986).
38. A. Anile, S. Pennisi, Phys. Rev. B 46, 13186 (1992)
39. R. Stratton, Phys. Rev. **126**, 2002 (1962)
40. S. Reggiani, M.C. Vecchi, M. Rudan, IEEE Trans. Electron. Devices 45, 2010 (1998)
41. N. Goldsman, L. Henrickson, J. Frey, Solid-state Electron. 34, 389 (1991)
42. A. Gnudi, D. Ventura, G. Baccarani, F. Odeh, Solid-state Electron. 36, 575 (1993)
43. S. Jin, A. Wettstein, W. Choi, F. M. Bufler, E. Lyumkis, in *2009 International Conference on Simulation of Semiconductor Processes and Devices* (IEEE, 2009a) pp. 1–4.
44. S. Jin, A. Wettstein, W. Choi, F. M. Bufler, E. Lyumkis, in *2009 International Conference on Simulation of Semiconductor Processes and Devices* (IEEE, 2009b), pp. 1–4.
45. G. Matz, S.-M. Hong, C. Jungemann, in *2010 International Conference on Simulation of Semiconductor Processes and Devices* (IEEE, 2010), pp. 167–170.
46. S.-M. Hong, G. Matz, C. Jungemann, IEEE Trans. Electron. Devices 57, 2390 (2010)
47. D. Rode, Phys. Rev. B 2, 1012 (1970)
48. D. Rode (Elsevier, 1975), vol. 10 of *Semiconductors and Semimetals*, pp. 1 – 89. http://www.sciencedirect.com/science/article/pii/S0080878408603312.
49. A.K. Mandia, R. Patnaik, B. Muralidharan, S.-C. Lee, S. Bhattacharjee, J. Phys.: Condens. Matter 31 (2019)
50. D. Howarth, E.H. Sondheimer, Proc. R. Soc. Lond. Ser. A. Math. Phys. Sci. 219, 53 (1953)
51. J. Appel, in *Solid State Physics* (Elsevier, 1968), vol. 21, pp. 193–391.
52. B. Floyd, Y. Le Coz, in *Computational Electronics* (Springer, 1991), pp. 93–95.
53. S. Krishnamurthy, M. van Schilfgaarde, in *Computational Electronics* (Springer, 1991), pp. 119–122.
54. R. W. Hockney, J. W. Eastwood, *Computer simulation using particles* (CRC Press, 1988).
55. C. Jacoboni, P. Lugli, *The Monte Carlo Method for semiconductor device simulation* (Springera, 2012).
56. P. J. Price, in *Semiconductors and semimetals* (Elsevier, 1979), vol. 14, pp. 249–308.
57. C. Jacoboni, L. Reggiani, Rev. Mod. Phys. 55, 645 (1983a)
58. A. Boardman, W. Fawcett, H. Rees, Solid State Commun. 6, 305 (1968)
59. W. Fawcett, A. Boardman, S. Swain, J. Phys. Chem. Solids 31, 1963 (1970)
60. K. Kometer, G. Zandler, P. Vogl, Semicond. Sci. Technol. 7, B559 (1992a)
61. K. Kometer, G. Zandler, P. Vogl, Phys. Rev. B 46, 1382 (1992b)
62. B. Niclot, P. Degond, F. Poupaud, J. Comput. Phys. 78, 313 (1988)
63. P. Degond, F. Guyot-Delaurens, J. Comput. Phys. 90, 65 (1990)
64. J. McKelvey, R. Longini, T. Brody, Phys. Rev. 123, 51 (1961)
65. A. Das, M.S. Lundstrom, Solid-state Electron. 33, 1299 (1990)
66. M.A. Stettler, M.S. Lundstrom, Appl. Phys. Lett. 60, 2908 (1992)
67. H. Budd, J. Phys. Soc. Jpn 21 (1966)
68. P. Price, IBM J. Res. Dev. 14, 12 (1970)
69. D. Ferry, J. Appl. Phys. 50, 1422 (1979)
70. J.G. Ruch, IEEE Trans. Electron. Devices 19, 652 (1972)
71. M. Heiblum, M. Nathan, D.C. Thomas, C. Knoedler, Phys. Rev. Lett. 55, 2200 (1985)
72. M.S. Shur, L.F. Eastman, IEEE Trans. Electron. Devices 26, 1677 (1979)
73. W.A. Hadi, M.S. Shur, S.K. O'Leary, J. Appl. Phys. 112 (2012a)
74. W.A. Hadi, S. Chowdhury, M.S. Shur, S.K. O'Leary, J. Appl. Phys. 112 (2012b)
75. W.A. Hadi, M.S. Shur, S.K. O'Leary, J. Mater. Sci.: Mater. Electron. 24, 1624 (2013)
76. P. Wang, L. Hu, Y. Yang, X. Shan, J. Song, L. Guo, Z. Zhang, AIP Adv. 5 (2015)
77. H. Kim, H. Tian, K. Kim, M. Littlejohn, Appl. Phys. Lett. 61, 1202 (1992a)
78. D. Dolgos, H. Meier, A. Schenk, B. Witzigmann, J. Appl. Phys. 111 (2012)
79. C. Jacoboni, L. Reggiani, Rev. Mod. Phys. 55, 645 (1983b)
80. E. Conwell, M. Vassell, Phys. Rev. 166, 797 (1968)
81. O. Madelung, *Semiconductors: Data Handbook* (Springer, 2012).
82. K. Tomizawa, *Numerical Simulation of Submicron Semiconductor Devices* (Artech House, 1993).
83. J. Ruch, W. Fawcett, J. Appl. Phys. 41, 3843 (1970)
84. W. Fawcett, H. Rees, Phys. Lett. A 29, 578 (1969)
85. V. Borsari, C. Jacoboni, Physica Status Solidi (b) 54, 649 (1972).
86. J. M. Hammersley, D. Handscomb, *Dc (1984) Monte Carlo Methods*.
87. D. Vasileska, S.M. Goodnick, G. Klimeck, *Computational Electronics: Semiclassical and Quantum Device Modeling and Simulation* (CRC Press, 2017).
88. B.K. Ridley, *Quantum Processes in Semiconductors* (Oxford University Press, 2013).
89. K. Nederveen, Ph.D. thesis, Technische Univ., Eindhoven (Netherlands). (1989).
90. J. Singh, *Electronic and Optoelectronic Properties of Semiconductor Structures* (Cambridge University Press, 2007).
91. J. Hauser, M. Littlejohn, T. Glisson, Appl. Phys. Lett. 28, 458 (1976)
92. M.V. Fischetti, IEEE Trans. Electron. Devices 38, 634 (1991)
93. H. Kim, H. Tian, K. Kim, M. Littlejohn, Appl. Phys. Lett. 61, 1202 (1992b)
94. L. Keldysh, Sov. Phys. JETP 37, 509 (1960)
95. R. Curby, D. Ferry, Physica Status Solidi (a) 15, 319 (1973).
96. T. Wang, K. Hess, J. Appl. Phys. 56, 2793 (1984)

97. C. Palermo, L. Varani, J.-C. Vaissière, J.-F. Millithaler, E. Starikov, P. Shiktorov, V. Gružinskis, B. Azaïs, in *AIP Conference Proceedings* (American Institute of Physics, 2005), vol. 780, pp. 151–154.
98. E. Furno, F. Bertazzi, M. Goano, G. Ghione, E. Bellotti, Solid-State Electron. 52, 1796 (2008)
99. E. Starikov, P. Shiktorov, V. Gružinskis, L. Reggiani, L. Varani, J. Vaissiere, C. Palermo, Semicond. Sci. Technol. **20**, 279 (2005)
100. F. Bonani, G. Ghione, in *Noise in Semiconductor Devices* (Springer, 2001), pp. 1–38.
101. A. El-Ela, A. Mohamed et al., Int. Schol. Res. Not. (2013)
102. B. Foutz, S. O'Leary, M. Shur, L. Eastman, MRS Online Proc. Libr. Arch. 512 (1998)
103. B.E. Foutz, S.K. O'Leary, M.S. Shur, L.F. Eastman, J. Appl. Phys. 85, 7727 (1999)
104. K. Seeger, *Semiconductor Physics*, 3rd edn. (Springer, 1985).
105. K. Cheng, A. Cho, W. Wagner, J. Appl. Phys. 52, 6328 (1981)
106. W.-P. Hong, A. Chin, N. Debbar, J. Hinckley, P. Bhattacharya, J. Singh, R. Clarke, Ph.D. thesis, American Vacuum Society (1987).
107. T. Tanahashi, K. Nakajima, A. Yamaguchi, I. Umebu, Appl. Phys. Lett. 43, 1030 (1983)
108. T. Maloney, J. Frey, J. Appl. Phys. 48, 781 (1977)
109. B. Nag, Bull. Mater. Sci. 13, 57 (1990)
110. I. Watanabe, T. Torikai, K. Makita, K. Fukushima, T. Uji, IEDL 11, 437 (1990)
111. W. Shockley, Solid State Electron. 2, 35 (1961)
112. G. Hill, P. Robson, W. Fawcett, J. Appl. Phys. 50, 356 (1979)
113. A.A. Quaranta, V. Borsari, C. Jacoboni, G. Zanarini, Appl. Phys. Lett. 22, 103 (1973)
114. S. K. O'eary, B. E. Foutz, M. S. Shur, L. F. Eastman, Solid State Commun. 150, 2182 (2010).
115. B. Foutz, L. Eastman, U. Bhapkar, M. Shur, Appl. Phys. Lett. 70, 2849 (1997)
116. W.A. Hadi, S. Chowdhury, M.S. Shur, S.K. O'Leary, J. Appl. Phys. 112 (2012c)

Publisher's Note Springer Nature remains neutral with regard to jurisdictional claims in published maps and institutional affiliations.